

---

# The Effect of Condensates and Inner Coatings on the Performance of Vacuum Hohlräum Targets

## Introduction

Inertial confinement fusion (ICF) targets for the National Ignition Facility (NIF)<sup>1</sup> consist of a cryogenic capsule containing frozen deuterium–tritium (DT) fuel inside a gold or uranium hohlraum.<sup>2</sup> High-power laser beams enter the cylindrical hohlraum through a hole in each end cap, heating the interior to a temperature of  $\sim 300$  eV (Ref. 3). This thermal radiation drives ablation of the capsule, causing it to implode and ignite the DT fuel. We report the results of experiments on the OMEGA laser<sup>4</sup> that support the national campaign to achieve ignition. These experiments used cryogenic hohlraums containing a sample of the ignition capsule ablator material and were driven to  $\sim 180$  eV.

Although the primary purpose of these OMEGA experiments was to study the shock-timing technique for NIF ignition targets, we observed and identified the cause of an interesting discrepancy between the x-ray drive in cryogenic and identical room-temperature hohlraums. Namely, peak drive temperatures were 15% lower in cryogenic hohlraums than in identical warm hohlraums, and the temporal history of the drive was also changed. Furthermore, laser–plasma interaction processes produce hard x rays ( $h\nu > 20$  keV) 100 $\times$  more abundantly in cryogenic targets. Spatial nonuniformities in the x-ray emission were also observed within cryogenic hohlraums.

The reduced performance of the cryogenic targets resulted from the condensation of background gases on the inner walls of the cryogenic hohlraums. This was confirmed when hohlraum targets coated with thin ( $\sim 2$ - $\mu\text{m}$ ) layers of CH reproduced the behavior of the cryogenic targets. The primary effect of low- $Z$  coatings (CH and condensates) is the reduction of x-ray conversion efficiency within the hohlraum. They also produce longer plasma scale lengths that cause laser–plasma instabilities, which reduce the absorption of the drive laser and produce hot electrons and x rays. These findings are important to some non-ignition hohlraums that use low- $Z$  liners<sup>5–8</sup> (or layers) on the inside hohlraum walls to tamp or resist the expansion of the laser-ablated wall material. In contrast, ignition hohlraums will be filled with a low- $Z$  gas to keep the laser entrance hole

open.<sup>9,10</sup> Windows are placed on the laser entrance holes to retain the gas; these windows also serve to protect the inside of the hohlraum from the deposition of condensates. Moreover, the NIF cryogenic targets are housed inside shrouds to minimize condensation until they open a few seconds before the shot. These OMEGA experiments confirm that eliminating condensation on cryogenic targets is crucial for optimal hohlraum performance.

## Experimental Configuration

A series of experiments were performed on the OMEGA Laser System to demonstrate a technique to time the multiple shock waves in the ignition targets planned for the NIF.<sup>11</sup> This study used gold hohlraum targets with re-entrant cones to diagnose the shock-wave trajectories. The hohlraums were empty (also termed vacuum hohlraums): they contained no gas nor did they have windows on the laser entrance holes. Both warm and cryogenic targets were used in these experiments. (In the cryogenic targets, the liquid deuterium was confined to the re-entrant cones and did not enter the hohlraum.)

The hohlraums were made of 25- $\mu\text{m}$ -thick Au, were 2.55 mm long and 1.6 mm in diameter, and contained 1.2-mm-diam laser entrance holes (LEH's). They were oriented along the P6–P7 axis of the OMEGA target chamber and driven with 38 OMEGA beams that had no beam smoothing (phase plates nor spectral dispersion) and were focused in three cones of beams (with different angles of incidence) in a standard configuration for hohlraums on OMEGA. The three cones of beams were five beams at 21°, five beams at 42°, and nine beams at 59° entering each end of the hohlraum (angles are relative to the hohlraum axis). These cones were each pointed along the hohlraum axis but outside the LEH by 0.725, 0.2, and 0 mm, respectively. They focused at 0.8, 0.5, and 0.0 mm (respectively) before these pointing positions. The drive pulse was a 2-ns temporally square pulse that produced spot intensities greater than  $10^{14}$  W/cm<sup>2</sup> on the inner surface of the hohlraum. Figure 120.22 shows the hohlraum and drive-beam configuration with the x-ray and optical diagnostics used in the experiments.

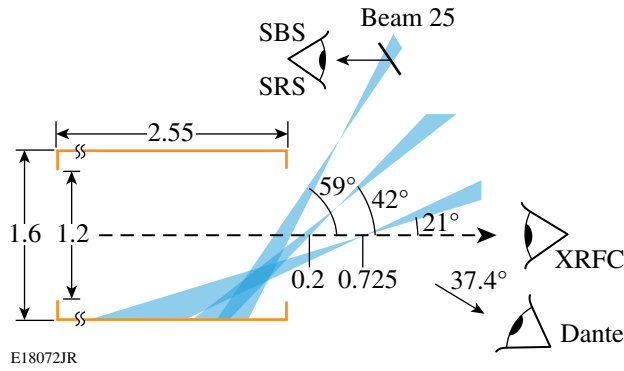


Figure 120.22  
The experimental configuration where hohlraum targets are irradiated at each end by three cones of beams at 21°, 42°, and 59°. X-ray diagnostics viewed the hohlraum through the laser entrance hole and optical diagnostics detected light scattered back through Beam 25, a 59° beam.

These experiments employed a suite of diagnostics to monitor the performance of the hohlraums. The radiation temperature within the hohlraum was measured using the Dante diagnostic:<sup>12–14</sup> an array of 12 x-ray diode detectors filtered to provide the x-ray emission in various bands of x-ray energies. The responses of the detectors were absolutely calibrated (temporally and in x-ray energy) so the diode current could be converted into a temporal history of the x-ray flux in the energy band determined by the filtration. By fitting these multi-energy measurements to a blackbody distribution, one can determine the equivalent radiation temperature within the hohlraum as a function of time.<sup>13,15</sup> Another array of four x-ray photomultiplier tubes measured the integrated energy of hard x rays, i.e., those above cut-off energies of 20, 40, 60, and 80 keV (Ref. 16).

A framing x-ray pinhole camera<sup>17</sup> (XRFC) viewed the hohlraum along the hohlraum axis through the LEH. This device uses pinholes backed by both soft x-ray mirrors and x-ray filters to provide images of the hohlraum at x-ray energies of  $h\nu = 0.5, 0.9, \text{ and } 1.5 \text{ keV}$ .

One of the drive-laser beams (Beam 25) has a diagnostic that records the temporal and spectral profiles of light reflected from the hohlraums back through the focus lens. This is done for two spectral regions: one near 351 nm (the drive-laser wavelength) and the other in the range 400 nm to 700 nm. These wavelength regions are used to diagnose the presence of stimulated Brillouin scattering (SBS) and stimulated Raman scattering (SRS), respectively. The total energy reflected back through the focus lens was measured with a calorimeter. These diagnostics were used to monitor the effects of nonlinear laser–plasma interaction processes that scatter the drive-laser light.

### Radiation Temperature

In these experiments a distinct difference was observed in the behavior of warm (ambient temperature) and cryogenic ( $T < 20 \text{ K}$ ) hohlraums. Figure 120.23 shows the radiation temperature (measured by Dante) in hohlraum targets as a function of laser drive energy. The upper red points are the measured peak radiation temperatures for warm hohlraums. The red curve is a  $T_{\text{rad}} \propto E^{0.25}$  power law fit to those data. All of these hohlraums had re-entrant diagnostic cones for the shock-timing experiments. In all but three, the tips of those cones were fitted with Be–Cu–Be sandwiches<sup>11</sup> that replicate the x-ray opacity of the ablator in an ignition capsule.<sup>18</sup> In Fig. 120.23, at ~12-kJ drive energy, three yellow squares show the radiation temperatures for identical hohlraum targets that had gold cone tips instead of

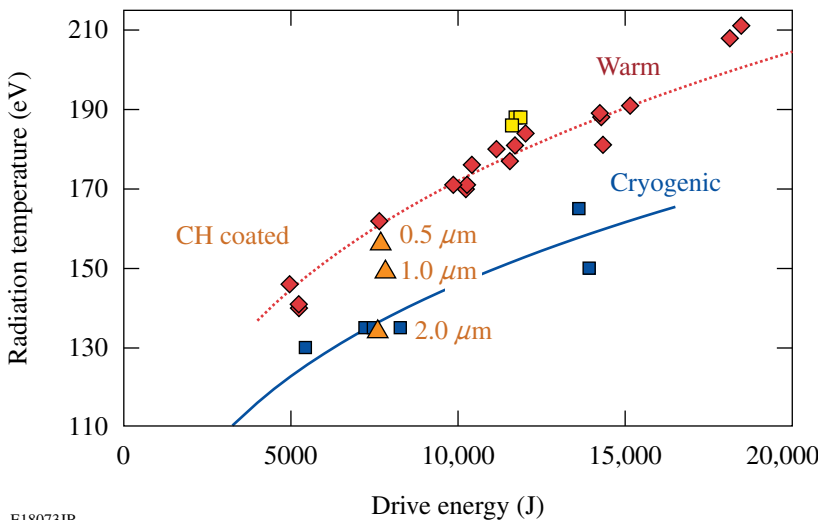


Figure 120.23  
Hohlraum radiation temperature (as measured by Dante) as a function of drive-laser energy for warm hohlraums (red diamonds) and cryogenic hohlraums (blue squares). The red and blue curves are  $T_{\text{rad}} \propto E^{0.25}$  fit to the warm and cold data. The three yellow squares at 12 kJ are targets with cone tips made of gold instead of Be–Cu. The orange triangles are warm hohlraums coated with CH in the thicknesses shown.

E18073JR

the Be–Cu sandwiches. These gold-tipped targets show slightly higher radiation temperatures than the other warm targets, demonstrating the sensitivity of the radiation temperature to materials within the hohlraum. The Be–Cu sandwiches had a surface area that was  $\sim 10\%$  of that of the hohlraum. The lower albedo of the Be surface reduces the x rays returned to the radiation field by that surface; therefore, when the Be sandwiches are replaced with gold, the radiation temperature rises.

The lower blue points and blue curve (again a  $T_{\text{rad}} \propto E^{0.25}$  fit) are the radiation temperatures for the cryogenic hohlraums. The hohlraums used for these data were identical to the ones discussed above: they were nominally empty and were fitted with the diagnostic cone. Liquid (cryogenic) deuterium filled the diagnostic cones but did not enter the hohlraum. The cryogenic targets show a 15% reduction in peak radiation temperature compared to identical warm ones.

Figure 120.24 shows the radiation temperature as a function of time for four experiments: two warm and two cryogenic. (The radiation temperatures plotted in Fig. 120.23 are the peak values of this type of data.) The upper bold and thin dotted lines are results for warm experiments performed at 14 kJ (shot 47240) and 7.5 kJ (shot 47241), respectively. These data exhibit the standard profile for radiation temperature produced by a 2-ns square pulse: an initial fast rise as hot, low-density plasma

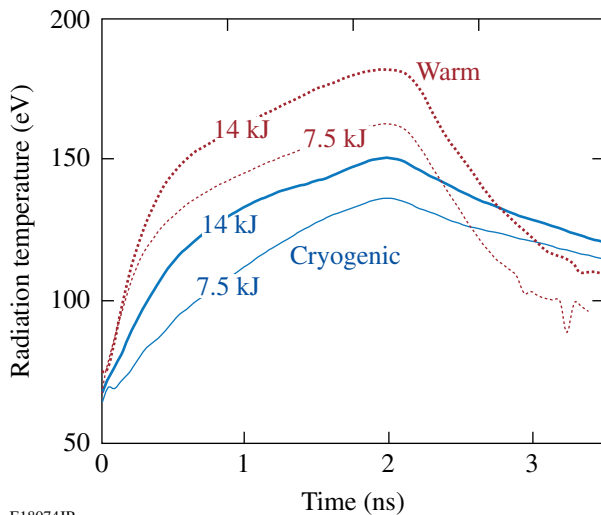


Figure 120.24

The temporal profile of the radiation temperature for four experiments: two warm targets (upper curves) at 14-kJ (bold dotted) and 7.5-kJ (thin dotted) drive energy and two cryogenic targets (lower curves) at 14-kJ (bold solid) and 7.5-kJ (thin solid) drive energy. The cryogenic targets show distinctly different behavior: lower rise times, lower peak temperatures, and decreased cooling rates.

is created and the laser deposits energy into this plasma. This is followed by a slow rise as a thermal x-ray–driven Marshak wave<sup>19</sup> moves into the gold wall, producing a rise in the wall albedo. When the drive-laser pulse ends, the radiation temperature has peaked and the hohlraum begins to cool at a rate determined by its geometry and the total heated mass contained in the hohlraum. The warm experiments exhibit identical behavior, differing only in their magnitudes.

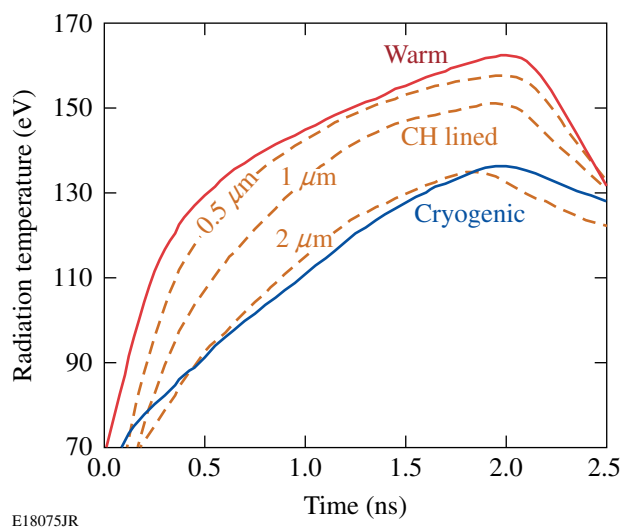
The lower bold and thin solid curves are the radiation-temperature profiles for identical targets cooled to cryogenic temperatures and driven by similar energies [14 kJ (shot 48884) and 7.5 kJ (shot 48881)]. These shapes are distinctly different than the warm targets but are similar to each other. Their rate of rise is much slower, their peak temperatures are lower, and they cool at a significantly slower rate than the warm targets. The performance of the cryogenic hohlraums is reduced compared to warm ones: the peak temperatures are lower and the response time is slower.

### Effect of CH Coatings

The differences between the warm and cryogenic targets appear to be the result of condensation layers that form on the inner walls of the cryogenic hohlraums. The cryogenic targets were mounted on the cold finger of a sizable cryogenic system<sup>20</sup> that connects to the OMEGA target chamber and has its own vacuum system. Targets were installed in the cryogenic system, which was evacuated (separately from the target chamber), and then the targets were cooled. As a result, the cryogenic hohlraum targets spent 20 to 50 min at temperatures below 70 K, where the pressure was  $\geq 10^{-5}$  Torr. At these temperatures, background gases will condense on the cold surfaces. Residual gas analysis on the vacuum systems show that the background gases in these systems were comprised predominantly of water vapor, nitrogen, and oxygen.

In low-mass cryogenic targets, a protective shroud is frequently used to shield the target from thermal radiation. The cold surfaces of the shroud act as cryogenic pumps that produce lower pressure in the vicinity of the target. This reduces the level of background gas that can condense onto the cold target. The thermal mass of the cold finger for these hohlraum targets was sufficient to prevent heating by background radiation. For expediency the cryogenic hohlraum targets were fielded *without* a protective shroud. The targets easily maintained temperatures to produce liquid deuterium but were likely exposed to increased condensates. Simple estimates for condensation rates at the applicable pressures indicate that these targets could have had several microns of condensed material on them.

To test whether the behavior of the cryogenic targets resulted from condensation, hohlraums (identical to those described above) were lined with thin layers of parylene (CH) and irradiated in the same manner as the warm hohlraum targets. The results of three experiments with CH-lined targets are shown in Fig. 120.23 as orange triangles at  $\sim 7.8$  kJ. Note that as the CH-coating thickness increases (0.5, 1.0, and 2.0  $\mu\text{m}$ ), the radiation temperature decreases, ultimately matching the cryogenic target results quite closely. This progression and the replication of the behavior of cryogenic targets are shown in Fig. 120.25 as another plot of radiation temperature as a function of time. The upper and lower curves are the thin curves from Fig. 120.24 for warm (red) and cryogenic (blue) targets. The data (orange) for the CH-lined target show that as the CH-coating thickness increases, the temporal profile better replicates the cryogenic target's behavior: The rate of rise decreases, the peak radiation temperature decreases, and the cooling time increases. The data for the 2- $\mu\text{m}$  CH coating closely replicate the behavior of the cryogenic hohlraums, suggesting that the cryogenic targets have a condensation layer that is equivalent to  $\sim 2$   $\mu\text{m}$  of CH. [These CH-coated data are also consistent with previous results for hohlraums lined with 0.44  $\mu\text{m}$  of CH (Ref. 21).]



E18075JR

Figure 120.25

The effect of CH coatings on the temporal profiles of radiation temperatures. Profiles for warm and cryogenic hohlraum targets driven at 7.5 kJ are the red and blue curves (from Fig. 120.24). The orange curves depict the profiles for hohlraums with CH coatings of 0.5-, 1.0-, and 2.0- $\mu\text{m}$  thicknesses.

### X-Ray Emission

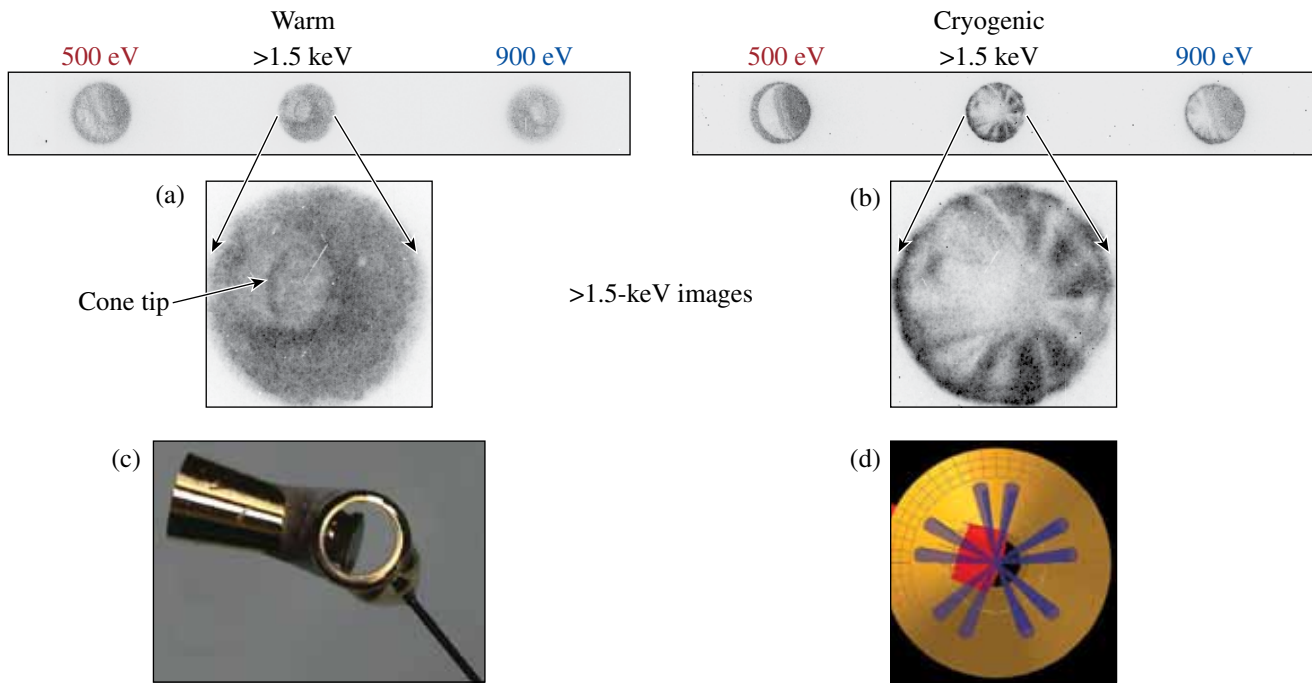
Figure 120.26 shows time-gated x-ray pinhole camera images of the targets, viewed through the LEH, for two shots: (a) a warm hohlraum driven by 14.2 kJ (shot 48879) and (b) a

cryogenic hohlraum driven by 13.9 kJ (shot 48884). In both figures the left and right images were formed with 500-eV and 900-eV radiation, respectively. The center images were formed with radiation greater than 1.5 keV. For those lower-energy images, spectral discrimination was obtained with grazing-incidence mirrors; for the  $>1.5$ -keV image, a simple transmission filter was used. As a result, the left and right images are inverted (left for right) with respect to the center image. Note that the  $<1$ -keV x-ray images in both warm and cryogenic experiments are fairly uniform, as is the  $>1.5$ -keV x-ray image for the warm hohlraum. In contrast, the  $>1.5$ -keV x-ray image of the cryogenic hohlraum has significant structure.

The enlarged images are those at  $h\nu > 1.5$  keV for (a) the warm and (b) the cryogenic experiments. The warm image has a fairly uniform emission profile within the hohlraum, and one can discern the outline of the lower-albedo Be cone tip. [For reference, Fig. 120.26(c) is an image of a hohlraum target through the LEH along the same direction as the framing camera that produced the images in Figs. 120.26(a) and 120.26(b).] The image of the cryogenic experiment exhibits strongly structured emission in radial spokes that are triangular in shape. This structure has a configuration similar to the pointing arrangement of a subset of the incident laser beams.

Three cones of laser beams enter the hohlraum through the LEH at angles of 21°, 42°, and 59° with respect to the hohlraum axis. The outer nine beams (at 59°) were pentagonally arranged with two beams on each edge (minus one beam not used in these experiments). Because of their steep angle of incidence, these beams are closest to the LEH and the x-ray emission from their spots is most visible from outside the hohlraum. Figure 120.26(d) is a simple drawing of the target and LEH showing the outer beams from their focal point (on the hohlraum axis) to the hohlraum wall. They are pointed at the center of the LEH but come to focus 0.8 mm before that point. The beams are diverging so the blowoff plasma flows into higher laser intensity as it expands off the hohlraum wall. Lastly, the low-Z material expanded more rapidly than the gold, therefore extending farther into the beam path.

The enlarged image in Fig. 120.26(b) shows the similarity to that beam configuration, with the dark areas representing the beam profiles where the x rays were created. Only eight beams appear in the image because one beam interacted obliquely with the diagnostic cone and had reduced x-ray brightness. X-ray images of the CH-lined targets exhibit spoke-like features similar to those in the cryogenic targets, as shown in Fig. 120.26(b).



E18076JR

Figure 120.26

Framing x-ray pinhole camera images the hohlraum targets through the LEH and along the hohlraum axis for (a) a warm hohlraum target and (b) a cryogenic hohlraum target. The data for each comprise three images, each taken at 1.8 ns. The image on the left is 500-eV radiation and the right is 900-eV radiation. The center was radiated with  $h\nu > 1.5$  keV. (The 1.5-keV images are expanded for clarity.) (c) Image of the hohlraum target through the LEH [at same view as that of Figs. 120.26(a) and 120.26(b)] showing the configuration of the hohlraum and VISAR cone. (d) Drawing of the LEH with the outlines of the outer cone of beams superposed. The x-ray emission in (b) has a similar structure.

### Reflected Light and Hard X-Ray Measurements

The full-aperture backscatter diagnostics on Beam 25 (FABS25) resolve light scattered into the  $f/6$  focusing optics temporally and spectrally in two wavelength bands, corresponding to stimulated Brillouin scattering (SBS,  $351 \pm 2$  nm) and stimulated Raman scattering (SRS, 400 nm to 700 nm). The temporal and spectral resolutions in these bands are typically  $\sim 40$  ps and  $\sim 0.04$  nm for the SBS channel and  $\sim 100$  ps and  $\sim 15$  nm for the SRS channel. All time-resolved spectra are shown in false-color images on logarithmic scales. The laser pulse shapes and the normalized, spectrally integrated scattered powers (Fig. 120.27) are superposed on the spectra in black and white, respectively. The SBS spectra also show a weak, narrow unshifted spectral component at 351 nm, caused by stray drive-laser light that misses the target.

Figure 120.27 shows SBS spectra for three hohlraum experiments: (a) a room-temperature hohlraum and (b) a cryogenic hohlraum, both driven at 14 kJ, and (c) a room-temperature hohlraum driven at 7.9 kJ. All hohlraum targets were gold and the hohlraum in Fig. 120.27(c) had a  $2\text{-}\mu\text{m}$  layer of CH.

The corresponding SRS spectra are shown in Fig. 120.28. The intensity of Beam 25 at the LEH is estimated to be between  $2$  and  $4 \times 10^{15}$  W/cm<sup>2</sup>. While a simple, uncoated gold hohlraum is not expected to have very much plasma near the LEH during most of the laser pulse, a hohlraum with low-Z layers (CH or condensates) may well have significant plasma near the LEH at early times. (This results from high-velocity blowoff from the hohlraum interior and from the edge of the LEH.) The highly blue shifted SBS signal early in Fig. 120.27(b) could result from a plasma that is rapidly expanding (highly supersonic) toward the laser. Alternatively, the incident light could be rapidly blue shifted as the result of a lateral influx of plasma into the beam.<sup>22</sup>

The broad bandwidth could be caused by strong coupling effects (high intensity near the LEH) but may also be associated with varying plasma conditions within the beam. The backscatter energies for both SBS and SRS for the three shots shown in Fig. 120.27 are given in Table 120.I, along with typical intensities at the LEH and at the hohlraum wall for Beam 25.

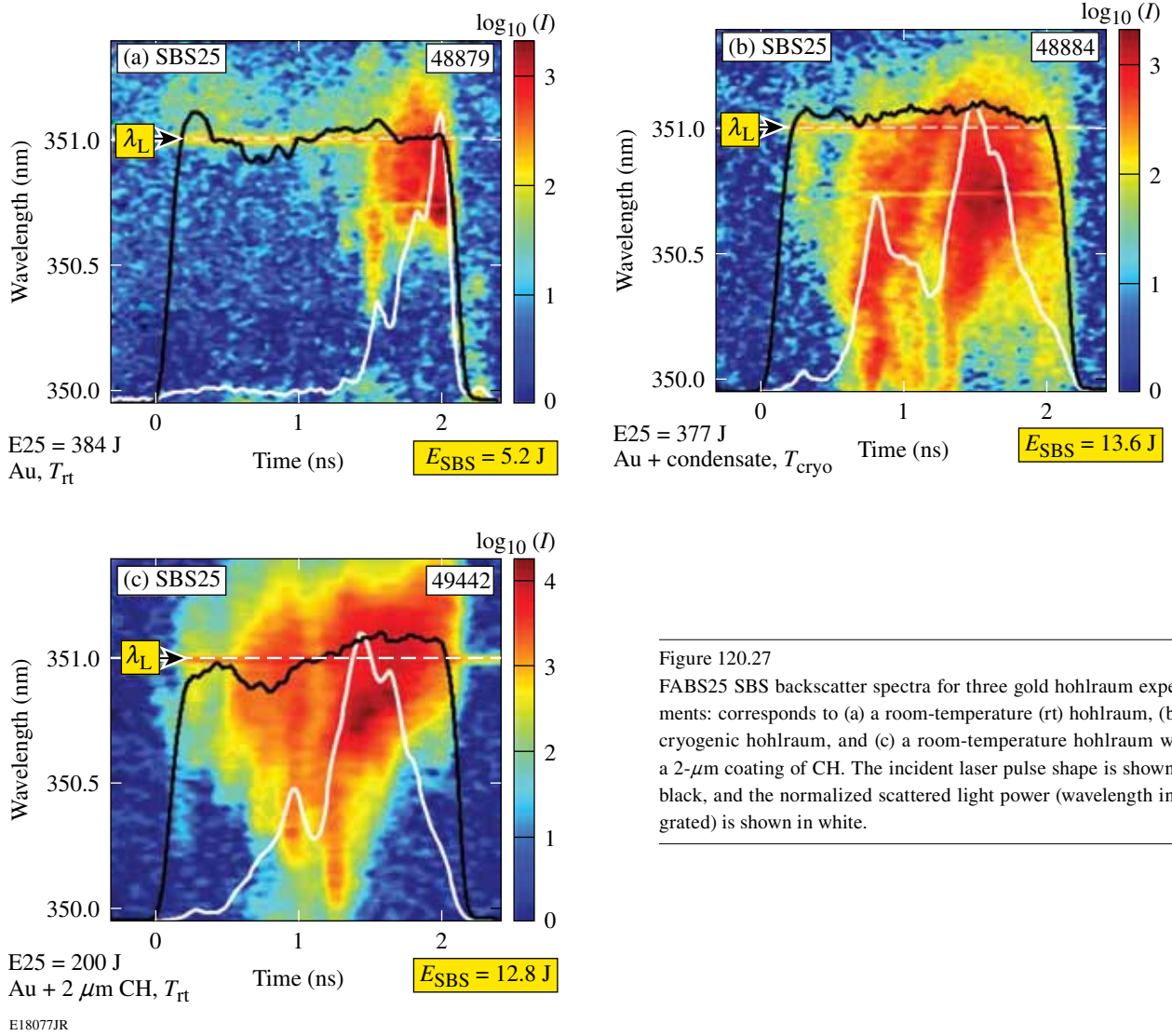


Figure 120.27  
 FABS25 SBS backscatter spectra for three gold hohlraum experiments: corresponds to (a) a room-temperature (rt) hohlraum, (b) a cryogenic hohlraum, and (c) a room-temperature hohlraum with a 2- $\mu\text{m}$  coating of CH. The incident laser pulse shape is shown in black, and the normalized scattered light power (wavelength integrated) is shown in white.

Table 120.I: SBS and SRS backscatter energies and reflectivities.

Shot Number	$I_{LEH}$	$I_{wall}$	$E_{SBS}$ (J)	$E_{SRS}$ (J)
48879 (warm)	2 to $4 \times 10^{15} \text{ W/cm}^2$	5 to $10 \times 10^{14} \text{ W/cm}^2$	5 J (1.3%)	1.5 J (0.4%)
48884 (cryo)	2 to $4 \times 10^{15} \text{ W/cm}^2$	5 to $10 \times 10^{14} \text{ W/cm}^2$	13.6 J (3.6%)	19 J (5%)
49442 (CH-lined)	1 to $2 \times 10^{15} \text{ W/cm}^2$	2 to $5 \times 10^{14} \text{ W/cm}^2$	12.8 J (6.4%)	13 J (6.6%)

The SRS spectra indicate that the main part of this backscatter radiation emanates from density regions that are 12%–14% of  $n_c$ , where  $n_c$  is the critical density ( $n_c = 10^{22} \text{ cm}^{-3}$  for  $\lambda_L = 351 \text{ nm}$ ). [The wavelength scale shown in Fig. 120.28(a) was converted to a density scale in Fig. 120.28(c) based on the plasma-wave dispersion relation for  $T_e = 2 \text{ keV}$ . The temperature correction is essentially negligible.] We conjecture that these relatively high densities are likely located close to the hohlraum wall inside the hohlraum and not at the LEH. There is extremely little SRS radiation for the room-temperature gold hohlraum, while significant SRS is observed for both the cryogenic gold hohlraum and the CH-coated room-temperature hohlraum.

Figure 120.29 shows the energy reflected back into Beam 25 as a function of incident beam energy. The warm, unlined hohlraums reflect 0.3%–1% of the beam energy, whereas

the cryogenic and CH-lined hohlraums reflect 3%–7%. It is noteworthy that each of the CH thicknesses has the same high reflectivity as the cryogenic targets; no intermediate behavior for the thinner coatings is observed.

Figure 120.30 shows the total hard x-ray signal (in the  $h\nu > 20\text{-keV}$  channel) as a function of total incident laser energy for the various targets. The hard x-ray signal increases dramatically ( $\propto E^7$ ) above a threshold that depends on the type of target: For warm, unlined hohlraums, the hard x-ray signal does not reach 1 pC until the drive energy is  $\sim 7.6 \text{ kJ}$ , whereas the cryogenic hohlraums reach that level at half that energy (3.8 kJ). For a given drive energy, the cryogenic hohlraums produce  $\sim 100\times$  the hard x-ray flux of the warm, unlined hohlraums. The CH-lined targets show an increase in hard x-ray production as compared to the unlined hohlraums, with the thinnest CH

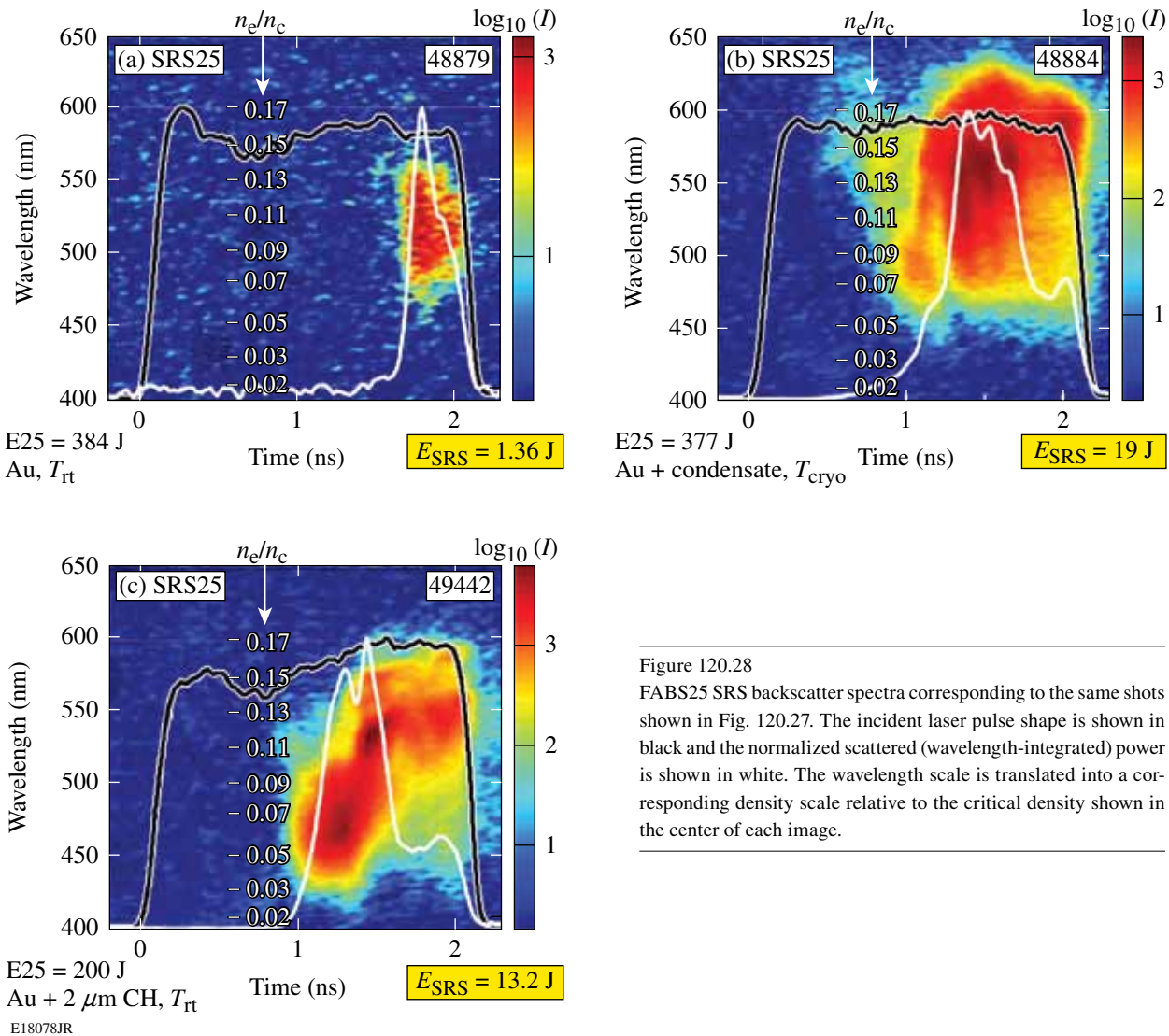


Figure 120.28  
FABS25 SRS backscatter spectra corresponding to the same shots shown in Fig. 120.27. The incident laser pulse shape is shown in black and the normalized scattered (wavelength-integrated) power is shown in white. The wavelength scale is translated into a corresponding density scale relative to the critical density shown in the center of each image.

coating producing 10× that of the unlined targets. Increased CH thickness increases the hard x-ray production: the 2- $\mu\text{m}$  case being 280× that of the uncoated warm target.

The radiation temperature results (Figs. 120.23 and 120.25) show that the CH-lined hohlraum replicates the behavior of the cryogenic hohlraums quite well. This effect is the result of the relatively low x-ray conversion efficiency of the low-Z materials (condensates and CH). Figures 120.29 and 120.30 show that there are some differences in the mechanisms by which condensates and CH coatings interact with the laser-scattered light and produce hard x rays. This is likely due to different materials (Z) of the two coatings affecting the plasma conditions and scale lengths. These laser-plasma coupling effects are small

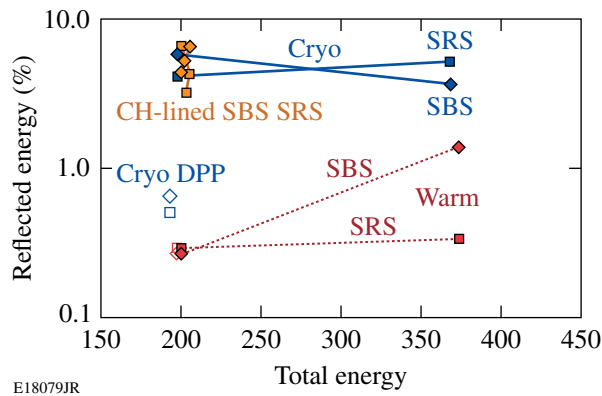


Figure 120.29  
The reflected energy (% of incident) in Beam 25 as a function of energy and for various target types. The warm, unlined hohlraums reflect 0.3%–1% of the beam energy; the cryogenic and CH-lined hohlraums reflect 3%–7%.

compared to that of the x-ray conversion but, nevertheless, can be important for the performance of hohlraum-driven targets because fast electrons and hard x rays are produced.

**Effect of Background Pressure**

In one cryogenic experiment the target-cooling procedure was changed. Instead of cooling the target within the ancillary vacuum in the cryogenic system, the target was not cooled until it reached the center of the OMEGA target chamber, where the pressure was considerably lower. Figure 120.31 compares the radiation-temperature temporal profiles of a warm target (black), a cryogenic target cooled in the cart (blue), and a cryogenic target (shot 49453) cooled at the center of the target

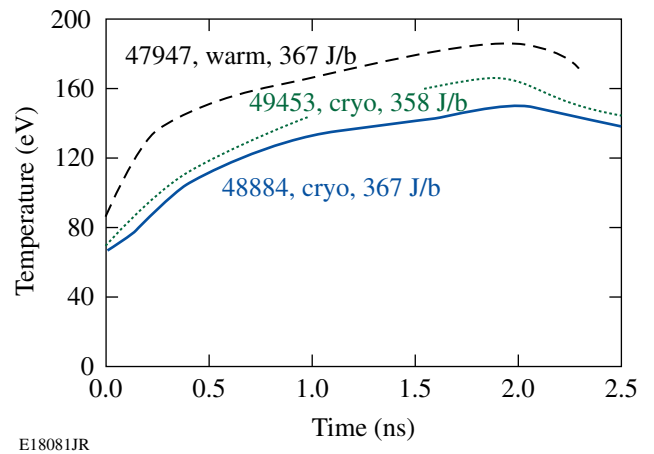
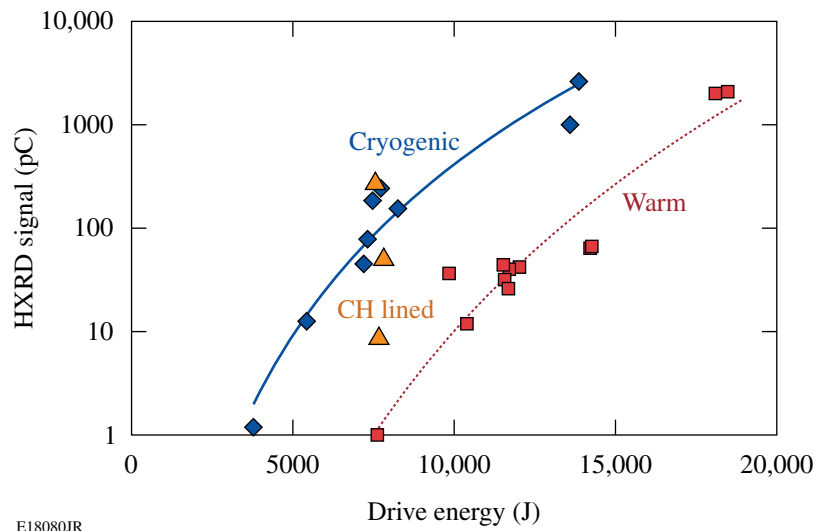


Figure 120.31  
Radiation temperature temporal profiles for a warm target (black), a cryogenic target cooled in the cart (blue), and a cryogenic target cooled at the center of the target chamber (green). The cart has a higher background pressure than the target chamber and therefore a greater deposition rate for condensates.

Figure 120.30  
Hard x-ray signal (in the  $h\nu > 20\text{-keV}$  channel) as a function of total incident laser energy for the various targets. The cryogenic, CH-coated targets produce more hard x rays than the warm, uncoated targets. This is a result of the long-scale-length plasmas that are created when the low-Z coating is present.



chamber (green). The target cooled in the target chamber shows a higher peak radiation temperature, and its rate of rise and cooling rates are incrementally closer to the behavior of the warm target. The peak radiation temperatures for these two shots are the cryogenic target data at 14 kJ in Fig. 120.23. These data and the CH-coated–target data confirm that the reduced performance in the cryogenic targets results from the condensation of background gases inside the cryogenic hohlraums. In the case of shot 49453, the reduced background pressure reduced the deposition rate of condensate, producing a thinner layer within the hohlraum. This manifested itself as higher radiation temperature and a temporal profile that is closer to that of a warm hohlraum.

**Effect of Focus Conditions**

Laser-beam smoothing is used to enhance laser-target coupling and reduce laser–plasma instabilities. The results discussed above show that the reduced performance of cryogenic and coated hohlraum is due primarily to the presence of low-Z material and that laser–plasma coupling is less important. This is demonstrated by hohlraum experiments performed with different focal positions and with beams having distributed phase plates (DPP’s)<sup>23,24</sup> in the drive-laser beams. In the former (“tight-focus case”), all of the targets were warm and all of the drive beams were pointed and focused at the center of the LEH. In the latter, the focus was the same as described above, but the beams were fitted with “elliptical” DPP’s that produced circular spots at the LEH.<sup>24</sup> The results for these experiments are shown in Fig. 120.32, a repeat of Fig. 120.23 with green triangles depicting the tight-focus case and the open red (warm) and blue (cryogenic) points depicting data from experiments using the DPP’s. Note that the tight-focus case exhibits a lower

radiation temperature in the warm targets. This is likely due to increased scattered-light fractions associated with the high intensities produced at the LEH by this beam configuration. This conclusion is supported by the apparent scaling suggested by the points at higher drive energies, which have even lower radiation temperatures with respect to the standard-focus case. As the intensity (energy) increases, so do the effects of laser–plasma instabilities. For the DPP case, note that the open data points replicate the respective behaviors of warm and cryogenic targets. The radiation temperature is still lower for cryogenic targets. Refer back to Fig. 120.30 and note the open data points; they represent experiments with DPP’s. Those data show that smoother beams (with DPP’s) reduce the scattered-light fractions in cryogenic targets but do not alter the hard x-ray production. These data indicate that the scattered-light fraction plays a small role in the reduction in radiation temperature for cryogenic and CH-coated targets.

**X-Ray Conversion Efficiency**

The Dante diagnostic provides a direct measure of time-resolved x-ray power emitted from the hohlraum target. One of the most striking results of these experiments is that the x-ray energy radiated from the hohlraum lined with 2 μm of CH is a factor of 2 lower than that from an unlined hohlraum. This is observed in both the peak and the instantaneous fluxes (as in Figs. 120.23 and 120.25, respectively).

The data show that cryogenic targets reflect about 5%–7%, but this is insufficient to explain the 15% reduction in radiation temperature. The blackbody radiation temperature scales roughly as the one-fourth power of the energy absorbed by the hohlraum. To produce a 15% reduction in the radiation tem-

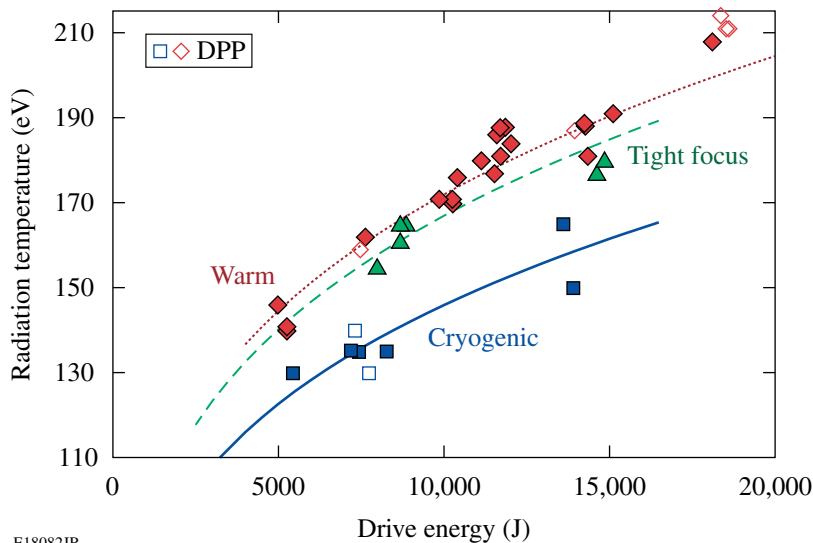


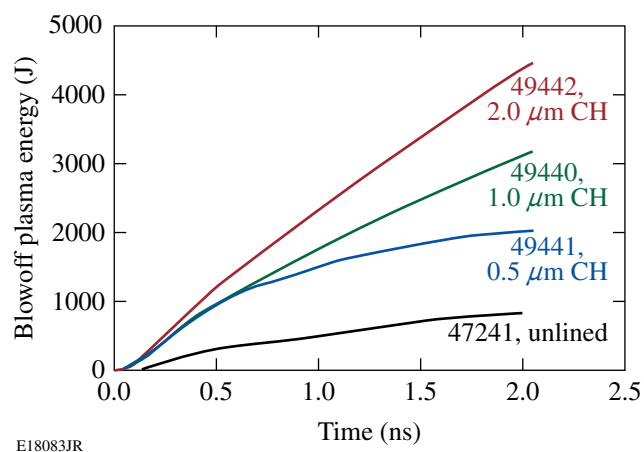
Figure 120.32  
Radiation temperature versus drive energy (repeat of Fig. 120.23) with data for “tight-focus case” (green triangles) and for experiments using the DPP’s with warm targets (red) and cryogenic targets (blue).

E18082JR

perature, the absorbed energy must be reduced to 50%. Instead, the reduction of radiation temperature is caused mainly by the addition of materials with low x-ray conversion efficiency. These materials interact with the laser and are heated but do not re-radiate x-ray energy as effectively as gold, so the radiation temperature is reduced.

Hohlraum targets have increased x-ray conversion efficiency<sup>2,25</sup> as compared to open (non-confined) targets, where the blowoff plasma is free to expand. In hohlraums, the plasma energy and mass accumulate within the hohlraum volume. Increased x-ray conversion efficiency results initially from the conversion of kinetic energy<sup>26</sup> but later is predominantly a result of emission from the accumulated material that is heated by the drive lasers. Experiments<sup>27</sup> show that the intensity of the x rays emitted from laser-irradiated plasmas in hohlraums is similar to that of open-geometry laser plasmas. The increase in hohlraum x-ray conversion efficiency, therefore, results from the confinement and heating of the gold blowoff plasma that creates larger regions of x-ray emission. When low-*Z* layers are added to hohlraums, they fill the hohlraum with a plasma that (a) does not emit x rays as efficiently as gold and (b) reduces the energy that ultimately reaches the gold wall. These significantly reduce the radiation temperature.

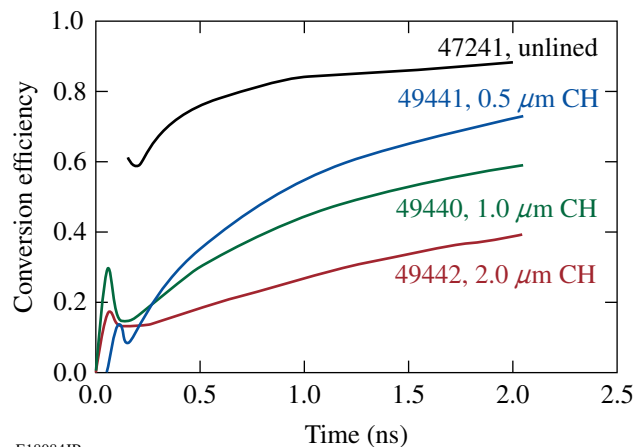
For the hohlraum radiation temperatures of interest in these experiments, the CH plasma (resulting from the 0.5- to 2.0- $\mu\text{m}$  CH liners) provides little opacity to thermal x rays from the gold walls. The x-ray power invested in the heating of the gold hohlraum wall can be approximated by  $(1-\alpha) A_w T^4$ , where  $T$  is the hohlraum temperature,  $A_w$  is the wall area, and  $(1-\alpha)$  is the absorbed x-ray fraction from the thermal-diffusion process [Eq. (2) of Ref. 28], based on the physics model for hohlraum energetics.<sup>29</sup> By implication, energy that is not radiated from the target, absorbed by the wall via penetration of the thermal wave, or directly backscattered from the target is therefore “lost” to the direct laser heating of the hot ( $>keV$ ), low-density blowoff plasma. Figure 120.33 shows a plot comparing this lost energy for comparably driven hohlraums with bare Au walls and CH liner thicknesses of 0.5, 1.0, and 2.0  $\mu\text{m}$ . In a hohlraum target, energy that directly heats the low-density, low-*Z* plasma constitutes inefficiency. A highly radiating plasma (e.g., gold) is advantageous, whereas a low-*Z* plasma tends to absorb the laser energy without significant re-radiation in the x-ray region. In Fig. 120.34, the measured radiation fluxes are recast into plots of x-ray conversion efficiency. It can be seen that the inferred x-ray conversion efficiencies reach levels as high as 85% in the unlined Au hohlraum but are reduced to as low as 50% in the hohlraum with the 2- $\mu\text{m}$  CH liner.



E18083JR

Figure 120.33

The plasma blow-off energy (or energy “lost”) as a function of time for bare (black) and CH-coated (blue, green, and red) hohlraums.



E18084JR

Figure 120.34

X-ray conversion efficiency as a function of time for bare (black) and CH-coated (blue, green, and red) hohlraums. Conversion efficiency is calculated from the x-ray flux (Dante) data.

## Simulations

These experiments were simulated using the radiation-hydrodynamics code LASNEX.<sup>30</sup> Figure 120.35 shows the simulated radiation temperature as a function of time for four hohlraum experiments: (a) uncoated and [(b)–(d)] coated with 0.5, 1.0, and 2.0  $\mu\text{m}$  of CH. The continuous curves are the simulations and the points (with error bars) are the Dante data. (These data are the warm and CH-lined data shown in Fig. 120.25 above.) The simulations model the radiation temperatures quite well. The magnitude and temporal behavior of each target are modeled as the effect of CH coatings, where

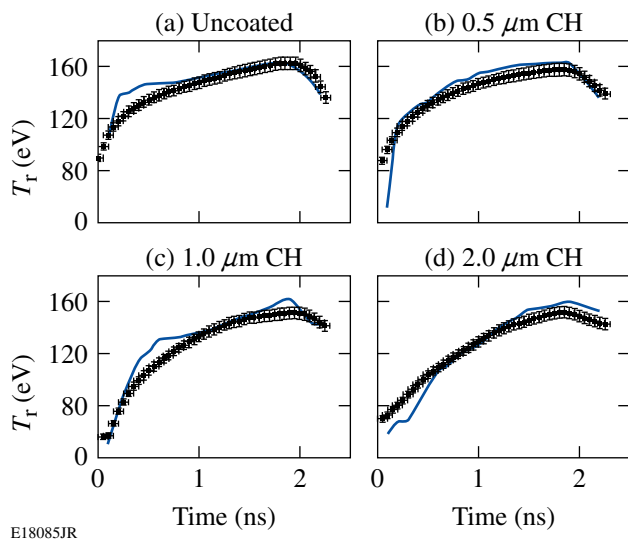


Figure 120.35

Simulation results for four warm hohlraum targets: (a) uncoated and coated with (b) 0.5, (c) 1.0, and (d) 2.0  $\mu\text{m}$  of CH. Note that the behavior of these radiation temperature profiles is quite similar to the experiments depicted in Fig. 120.25.

the reduced rise time, lower peak radiation temperature, and slower temperature decrease are all replicated. The experimental scattered-light signals were input into the simulations, so the primary effect modeled here is the reduced x-ray conversion efficiency and the hydrodynamics of the liner material.

### Summary

Experiments show that cryogenic vacuum hohlraums exhibit a significantly different behavior than identical warm hohlraums. The temporal profile of the radiation temperature for the cryogenic targets is changed with respect to the warm targets: early in the pulse the temperature rate of rise is lower, the peak temperature achieved is lower, and the cooling rate after the drive ceases is decreased. These observations are accompanied by significant changes in the x-ray emission structure within the hohlraum and by dramatic changes to the amount and character of the laser light that is reflected from the hohlraum.

For these experiments, the condensation of background gases onto the cold hohlraum surfaces is responsible for the degraded performance of the cryogenic hohlraums. This deposited material has lower x-ray conversion efficiency, which reduces the x-ray flux within the hohlraum. This affects the temporal rate of rise in the radiation temperature—its peak value. Experiments with identical warm hohlraum targets lined

with 2  $\mu\text{m}$  of CH replicated the behavior of the cryogenic hohlraum targets, confirming the effect of low-Z materials on the performance of hohlraum radiation temperature. The temporal profile of the radiation temperature in the lined targets was nearly identical to that of the cryogenic targets. This indicates that the cryogenic targets had a condensation layer equivalent to about 2  $\mu\text{m}$  of CH, which is consistent with estimates for the background gas that were present in the cryogenic system.

In addition to these radiation effects, the absorption of the drive-laser energy is reduced as a result of increased scattering caused by SBS and SRS. These instabilities produce hot electrons and hard x rays that can be detrimental to the performance of ICF targets. The temporal and spectral features of reflected light in the CH-lined targets were similar to that of the cryogenic targets, again confirming that the cryogenic targets contained layers of low-Z condensation.

These results are useful because they demonstrate the effect that low-Z layers have on the performance of laser-driven hohlraums. These effects are important for vacuum hohlraums, i.e., those without LEH windows or fill gases within the hohlraum. Ignition hohlraums at the National Ignition Facility will have both and are expected to be immune to these effects because background gases will be unable to condense on the hohlraum's inner surfaces and the fill gas will be of low-enough density to have little effect on x-ray conversion.

### ACKNOWLEDGMENT

This work was supported by the U.S. Department of Energy Office of Inertial Confinement Fusion under Cooperative Agreement No. DE-FC52-08NA28302, the University of Rochester, and the New York State Energy Research and Development Authority. The support of DOE does not constitute an endorsement by DOE of the views expressed in this article.

### REFERENCES

1. J. A. Paisner, E. M. Campbell, and W. J. Hogan, Lawrence Livermore National Laboratory, Livermore, CA, Report UCRL-JC-117397, NTIS Order No. DE95010923 (1994). Copies may be obtained from the National Technical Information Service, Springfield, VA 22161.
2. J. D. Lindl *et al.*, *Phys. Plasmas* **11**, 339 (2004).
3. S. W. Haan *et al.*, *Nucl. Fusion* **44**, S171 (2004).
4. T. R. Boehly, D. L. Brown, R. S. Craxton, R. L. Keck, J. P. Knauer, J. H. Kelly, T. J. Kessler, S. A. Kumpan, S. J. Loucks, S. A. Letzring, F. J. Marshall, R. L. McCrory, S. F. B. Morse, W. Seka, J. M. Soures, and C. P. Verdon, *Opt. Commun.* **133**, 495 (1997).
5. J. D. Lindl, *Laser Program Annual Report 1978*, Lawrence Livermore National Laboratory, Livermore, CA, Report UCRL-50055-78, 2-77 (1978).

6. S. Pollaine, *Laser Program Annual Report 1988*, Lawrence Livermore National Laboratory, Livermore, CA, Report XDIV-90-0054, 246 (1988).
7. A. R. Thiessen, *Laser Program Annual Report 1988*, Lawrence Livermore National Laboratory, Livermore, CA, Report XDIV-90-0054 (1988).
8. S. Pollaine, *Laser Program Annual Report 1990/1991*, Lawrence Livermore National Laboratory, Livermore, CA, Report UCRL-LR-116901-90/91, 214 (1991).
9. S. W. Haan *et al.*, *Phys. Plasmas* **2**, 2480 (1995).
10. W. J. Krauser *et al.*, *Phys. Plasmas* **3**, 2084 (1996).
11. T. R. Boehly, D. H. Munro, P. M. Celliers, R. E. Olson, D. G. Hicks, V. N. Goncharov, G. W. Collins, H. F. Robey, S. X. Hu, J. A. Marozas, T. C. Sangster, O. L. Landen, and D. D. Meyerhofer, *Phys. Plasmas* **16**, 056302 (2009).
12. H. N. Kornblum, R. L. Kauffman, and J. A. Smith, *Rev. Sci. Instrum.* **57**, 2179 (1986).
13. C. Decker, R. E. Turner, O. L. Landen, L. J. Suter, H. N. Kornblum, B. A. Hammel, T. J. Murphy, J. Wallace, N. D. Delamater, P. Gobby, A. A. Hauer, G. R. Magelssen, J. A. Oertel, J. Knauer, F. J. Marshall, D. Bradley, W. Seka, and J. M. Soures, *Phys. Rev. Lett.* **79**, 1491 (1997).
14. C. Sorce *et al.*, *Rev. Sci. Instrum.* **77**, 10E518 (2006).
15. R. L. Kauffman *et al.*, *Rev. Sci. Instrum.* **66**, 678 (1995).
16. C. Stoeckl, V. Yu. Glebov, D. D. Meyerhofer, W. Seka, B. Yaakobi, R. P. J. Town, and J. D. Zuegel, *Rev. Sci. Instrum.* **72**, 1197 (2001).
17. D. K. Bradley *et al.*, *Rev. Sci. Instrum.* **66**, 716 (1995).
18. S. W. Haan *et al.*, *Phys. Plasmas* **12**, 056316 (2005).
19. R. E. Marshak, *Phys. Fluids* **1**, 24 (1958).
20. *LLE Review Quarterly Report* **103**, 128, Laboratory for Laser Energetics, University of Rochester, Rochester, NY, LLE Document No. DOE/SF/19460-626, NTIS Order No. PB2006-106675 (2005). Copies may be obtained from the National Technical Information Service, Springfield, VA 22161.
21. S. H. Batha and J. R. Fincke, *Rev. Sci. Instrum.* **75**, 3934 (2004).
22. T. Dewandre, J. R. Albritton, and E. A. Williams, *Phys. Fluids* **24**, 528 (1981).
23. Y. Lin, T. J. Kessler, and G. N. Lawrence, *Opt. Lett.* **20**, 764 (1995).
24. S. P. Regan, D. D. Meyerhofer, T. C. Sangster, R. Epstein, L. J. Suter, O. S. Jones, N. B. Meezan, M. D. Rosen, S. Dixit, C. Sorce, O. L. Landen, J. Schein, and E. L. Dewald, *Bull. Am. Phys. Soc.* **51**, 68 (2006).
25. L. J. Suter *et al.*, *Phys. Plasmas* **3**, 2057 (1996).
26. J. Massen, G. D. Tsakiris, and R. Sigel, *Phys. Rev. E* **48**, 2073 (1993).
27. F. Ze *et al.*, presented at the 1993 Topical Conference on Physics of Radiatively Driven ICF Targets, Monterey, CA (1993).
28. R. E. Olson *et al.*, *Rev. Sci. Instrum.* **74**, 2186 (2003).
29. M. D. Rosen, *Phys. Plasmas* **3**, 1803 (1996).
30. G. B. Zimmerman and W. L. Kruer, *Comments Plasma Phys. Control. Fusion* **2**, 51 (1975); J. A. Harte *et al.*, *ICF Quarterly Report: Special Issue: Computational Advances in ICF*, 150, Lawrence Livermore National Laboratory, Livermore, CA, Report UCRL-LR-105821-96-4 (1996).